

# Detached-Eddy Simulation Procedure Targeted for Design

Roger L. Davis\*

*University of California, Davis, Davis, California 95616*

and

John F. Dannenhoffer III<sup>†</sup>

*Syracuse University, Syracuse, New York 13244*

DOI: 10.2514/1.36680

**A new detached-eddy simulation procedure, MBFLO, is described for the simulation of turbulent flow over/within arbitrary geometry. This new procedure represents the first step toward developing a turbulent technique that reduces the reliance on traditional turbulence modeling by directly solving for the larger-scale turbulence effects in regions where the computational grid is sufficient to resolve those scales. A goal of this effort was to develop a detached-eddy simulation procedure for which the time-averaged solution can replace current steady simulation results for design. Because detached-eddy simulation requires the solution of the unsteady Navier–Stokes equations on computational grids that are typically an order in magnitude more dense than their Reynolds-averaged counterparts, special care was taken to make this new procedure computationally efficient. This paper describes the data structure, parallelization, and automation techniques used to produce time-averaged detached-eddy simulation predictions. Results for the turbulent flow through a turbine and compressor cascade at design and offdesign conditions, respectively, are shown to illustrate the technique.**

## Nomenclature

$E$	=	total energy
$g$	=	acceleration due to gravity
$H$	=	total enthalpy
$h$	=	static enthalpy
$I$	=	rothalpy
$k$	=	turbulent kinetic energy
$Pr$	=	Prandtl number
$Pr_t$	=	turbulent Prandtl number
$p$	=	pressure
$R$	=	radius from specified axis of rotation
$S_{ij}$	=	mean strain-rate tensor
$u$	=	axial velocity component
$\hat{u}$	=	internal energy
$V$	=	velocity magnitude
$v$	=	tangential velocity component
$z$	=	elevation
$\mu$	=	coefficient of viscosity
$\mu_\tau$	=	turbulent coefficient of viscosity
$\rho$	=	density
$\tau_{ij}$	=	shear stress tensor
$\Omega$	=	rotational velocity about specified axis of rotation, rad/s
$\omega$	=	turbulent dissipation rate divided by turbulent kinetic energy

## I. Introduction

**R**EYNOLDS-AVERAGED Navier–Stokes (RANS) solution procedures are routinely used for the prediction of steady or unsteady flows for a wide variety of geometry. For many applications, RANS solutions are adequate in terms of both solution

accuracy and computational turnaround time. Solution accuracy has been steadily improved from developments in turbulence modeling and increases in computational grid density allowed by parallelization techniques. Solution speed has been improved from advances in numerical techniques, computer hardware, and parallelization. If one were to quantify the general prediction accuracy of RANS simulations [1], they would find that performance, durability, and stability predictions are generally accurate to within 3–5% of measured values, given the typical time and resource constraints for solution turnaround today. This level of accuracy is sufficient for many applications. However, the use of automated design optimization and advanced design techniques for high-performance applications requires an increasing level of accuracy in order to differentiate designs, thereby requiring that the computational fluid dynamics (CFD) predictions become accurate to within 0.1% of the measured performance values. The challenge is to reach this new level of accuracy without sacrifices in solution turnaround time.

Research to move to this higher level of accuracy has been ongoing by a number of CFD development teams. Research topics have focused on high-order numerical schemes [2–6], parallelization techniques [7,8], and turbulence modeling for Reynolds-averaged [9–12], detached-eddy [13,14], and large-eddy simulation [15–18] procedures. The focus of the current effort has been to develop a new parallel detached-eddy simulation (DES) Navier–Stokes procedure that can produce time-averaged unsteady simulations in approximately the same turnaround time as previous Reynolds-averaged steady Navier–Stokes simulations. To reduce the reliance on traditional turbulence models that tend to break down in regions of mixing, a detached-eddy or hybrid RANS/LES model is used to directly solve for the transport of large-scale viscous flow structures while maintaining the traditional RANS turbulence model for small-scale and near-wall structures. Automation and parallelization techniques are incorporated to enable unsteady and time-averaged solutions to be obtained in an acceptable turnaround time.

## II. Governing Equations and Boundary Conditions

The unsteady Favre-averaged governing flowfield equations for an ideal compressible gas in the right-hand Cartesian coordinate system using relative-frame primary variables can be written as

Presented as Paper 534 at the 46th Aerospace Sciences Meeting, Reno, NV, 7–10 January 2008; received 15 January 2008; revision received 6 June 2008; accepted for publication 20 June 2008. Copyright © 2008 by the American Institute of Aeronautics and Astronautics, Inc. All rights reserved. Copies of this paper may be made for personal or internal use, on condition that the copier pay the \$10.00 per-copy fee to the Copyright Clearance Center, Inc., 222 Rosewood Drive, Danvers, MA 01923; include the code 0748-4658/08 \$10.00 in correspondence with the CCC.

\*Professor, Mechanical and Aeronautical Engineering. Associate Fellow AIAA.

<sup>†</sup>Associate Professor, Mechanical and Aerospace Engineering. Associate Fellow AIAA.

Conservation of mass:

$$\frac{\partial \rho}{\partial t} + \frac{\partial(\rho u_i)}{\partial x_i} = 0 \quad (1)$$

Conservation of momentum:

$$\frac{\partial(\rho u_i)}{\partial t} + \frac{\partial(\rho u_j u_i)}{\partial x_j} + \frac{\partial p}{\partial x_i} = \frac{\partial \tau_{ji}}{\partial x_j} - \overline{S m}_i \quad (2)$$

Conservation of energy:

$$\frac{\partial E}{\partial t} + \frac{\partial(\rho u_j I)}{\partial x_j} = \frac{\partial}{\partial x_j} \left[ u_i \tau_{ij} + \left( \frac{\mu}{Pr} + \frac{\mu_t}{Pr_t} \right) \frac{\partial h}{\partial x_j} \right] \quad (3)$$

Total energy:

$$E = \rho \hat{u} + \frac{\rho V^2}{2} - \frac{1}{2} \rho (\Omega R)^2 \quad (4)$$

Rothalpy:

$$I = H - \frac{1}{2} (\Omega R)^2 = \frac{E + P}{\rho} \quad (5)$$

Enthalpy:

$$h = H - \frac{V^2}{2} = \hat{u} + \frac{P}{\rho} \quad (6)$$

Shear stress:

$$\tau_{ij} = (\mu + \mu_t) S_{ij} \quad (7)$$

Mean strain-rate tensor:

$$S_{ij} = \frac{1}{2} \left( \frac{\partial u_i}{\partial x_j} + \frac{\partial u_j}{\partial x_i} \right) - \frac{2}{3} \frac{\partial u_k}{\partial x_k} \delta_{ij} \quad (8)$$

The body-force vector  $S_{mi}$  in momentum equation (2) represents any body forces per unit volume, such as those due to rotation (Coriolis and centripetal):

Momentum source vector:

$$\overline{S m}_i = -2\rho(\bar{\Omega} \times V) - \rho\bar{\Omega} \times (\bar{\Omega} \times \bar{R}) \quad (9)$$

For instance, if the fluid domain rotates only about the  $x$  axis at a rotational speed  $\Omega$  and the radius to any point in the domain is  $R = (y^2 + z^2)^{1/2}$ , the circumferential angle at that point is  $\theta = \tan^{-1}(z/y)$ , with the additional geometric identities  $y = R \cos \theta$  and  $z = R \sin \theta$ , then the momentum source term vector becomes

Example momentum source vector:

$$\overline{S m}_i = \begin{bmatrix} 0 & (x \text{ direction}) \\ 2\rho\Omega w + \rho\Omega^2 y & (y \text{ direction}) \\ -2\rho\Omega v + \rho\Omega^2 z & (z \text{ direction}) \end{bmatrix} \quad (10)$$

Additional governing equations as developed by Wilcox [9,19,20] for the transport of turbulent kinetic energy and turbulence dissipation rate in regions of the flow where the computational grid or global time-step size cannot resolve the turbulent eddies can be written as

Turbulent kinetic energy transport:

$$\frac{\partial(\rho k)}{\partial t} + \frac{\partial(\rho u_j k)}{\partial x_j} = \left( \tau_{ij} - \frac{2}{3} \rho k \delta_{ij} \right) \frac{\partial u_i}{\partial x_j} - \beta^* \rho k \omega + \frac{\partial}{\partial x_j} \left[ \left( \mu + \sigma^* \frac{\rho k}{\omega} \right) \frac{\partial k}{\partial x_j} \right] \quad (11)$$

Turbulent frequency transport:

$$\frac{\partial(\rho \omega)}{\partial t} + \frac{\partial(\rho u_j \omega)}{\partial x_j} = \alpha \frac{\omega}{k} \left( \tau_{ij} - \frac{2}{3} \rho k \delta_{ij} \right) \frac{\partial u_i}{\partial x_j} - \beta^* \rho \omega^2 + \sigma_d \frac{\rho}{\omega} \frac{\partial k}{\partial x_j} \frac{\partial \omega}{\partial x_j} + \frac{\partial}{\partial x_j} \left[ \left( \mu + \sigma \frac{\rho k}{\omega} \right) \frac{\partial \omega}{\partial x_j} \right] \quad (12)$$

Subgrid coefficient of turbulent viscosity:

$$\mu_t = \frac{\rho k}{\omega} \quad (13)$$

In regions of the flow where the larger-scale eddies can be resolved with the computational grid, techniques borrowed from large-eddy simulation are used to represent the viscous shear and turbulent viscosity. The large-eddy subgrid model described by Smagorinsky [15] is modified according to the detached-eddy considerations described by Strelets [13] and Bush and Mani [14], in which the turbulent viscosity is determined with

Large-eddy coefficient of turbulent viscosity:

$$\mu_t = \rho l_{le} \sqrt{k} \quad (14)$$

where  $l_{le}$  is an eddy length scale proportional to the grid/time-step filter width  $\Delta$ :

$$l_{le} = \min \left( \frac{\sqrt{k}}{\omega}, \beta^* C_{des} \Delta \right) \quad (15)$$

In addition, the dissipation term  $\beta^* \rho k \omega$  of the turbulent kinetic energy transport equation (11) is limited by the eddy length scale  $l_{le}$ , according to kinetic energy dissipation:

$$\beta^* \rho k \omega \Rightarrow \beta^* \rho k \max \left( \omega, \frac{\sqrt{k}}{\beta^* C_{des} \Delta} \right) \quad (16)$$

where  $C_{des}$  is a proportionality coefficient with a value on the order of 1.0. Based on a limited number of validations performed thus far, the  $C_{des}$  coefficient appears to be a function of the freestream Reynolds number based on the geometric characteristic length. Further validation simulations are necessary to determine this Reynolds number relationship.

The boundary conditions used during the solution of Eqs. (1–16) can be categorized into inlet, outlet, periodic, and solid-wall regions. At the inlet, the relative total pressure and total temperature are held fixed for the flow equations, and the turbulent kinetic energy and dissipation frequency are held at freestream levels that are a function of the specified freestream turbulence intensity and the dissipation length scale. At the exit, the static pressure is held fixed for the flow equations and the turbulent kinetic energy and dissipation frequency are extrapolated. Both inlet and exit boundary conditions are implemented in a manner to minimize reflections. Periodicity of the flow variables exist on the upper and lower boundaries of the computational domain upstream of the leading edge and downstream of the trailing edge for cascade geometry. The flow variables at a given point on a periodic boundary are held to be the same as the flow variables at a corresponding point on the opposing periodic boundary. In the current investigation, all solid walls were assumed to be adiabatic. The same boundary conditions were used for Reynolds-averaged and detached-eddy simulations.

### III. Numerical Techniques

The conservation equations given in Eqs. (1–3), (11), and (12) are solved using a Lax–Wendroff control-volume time-marching scheme as developed by Ni [21], Dannenoffer [22], and Davis et al. [23,24]. Numerical solution of unsteady flows can be performed with either the explicit [21] or a dual-time-step procedure [25]. These techniques are second-order-accurate in time and space. A multiple-grid convergence acceleration scheme [21] is used for steady Reynolds-averaged solutions and the inner convergence loop of

unsteady simulations using the dual-time-step scheme. The new approach is called MBFLO and has 2-D, axisymmetric (with and without swirl), and 3-D versions. The two-dimensional procedure MBLO2P (two-dimensional, parallel) and numerical results are described here.

It is recognized that two-dimensional detached-eddy simulations lack the three-dimensional effects resulting from the interaction of eddies in the third dimension [26] and therefore tend to underpredict diffusion. However, two-dimensional design is an important part of the overall design process of wings, turbomachinery blades, and other similar lifting bodies, and so a robust two-dimensional simulation capability is highly desirable. The hope is to account for the three-dimensional eddy-interaction effects through additional modeling in the future.

#### A. Data Structure

A multiblock point-matched structured-grid strategy is used in the current procedure. Blocks are constructed from multiple faces. Each face of a block is allowed to have an arbitrary number of subfaces to enable virtually any connectivity of blocks and any combination of boundary conditions along a face of a block. Blocks may have any arbitrary orientation relative to the adjoining blocks. Block-connectivity and boundary-condition information is defined by a global connectivity file that stores global block number, block rotational speed, and information for each subface of each face. The subface information includes the physical-boundary-condition type or the adjoining block number, the starting and ending indices of the subface, the starting and ending indices of the adjoining subface, and any auxiliary physical-boundary-condition information. The block-connectivity file is either constructed by the user or automatically produced by a grid-generation procedure.

#### B. Control of Numerical Dissipation

A new approach to numerical dissipation is introduced in the MBFLO codes. In central-difference codes, artificial dissipation is used to control odd-even decoupling and to capture shocks. The combined second- and fourth-difference dissipation model of Jameson et al. [27] is used in the current procedures for both the mean flow and turbulence transport equations. It is a common practice to decay, or scale, the numerical dissipation through the viscous flow regions so that the numerical dissipation does not overwhelm the conservation equation fluxes. Various approaches have been used previously to perform this function. Jameson et al. [27] suggested scaling the dissipation fluxes by the time step multiplied by the spectral radius. This scaling essentially decays the numerical smoothing based on the local minimum grid spacing. Thus, in regions of fine-grid spacing such as in the boundary-layer regions, the numerical dissipation is decreased. The disadvantage to this approach is that viscous flow regions, including wakes or large-eddy structures, often occur in regions where the computational grid is not clustered. As a result, the structure and physical effects of these viscous flows can be damped. Chima [28] decayed numerical dissipation through the viscous flow regions using a Mach number function. The disadvantage of using either a velocity or Mach number function is that inviscid regions of low-speed or low Mach number flow can often exist in the domain. As a result, the numerical dissipation can be decayed in regions where it should not. Davis et al. [23,24] decayed the numerical dissipation through boundary layers by determining the boundary-layer length scales and then decaying the numerical dissipation using exponential functions. This approach works well for boundary-layer flows, but unfortunately does not address the need to decay the numerical dissipation in general viscous flow regions.

In the current MBFLO procedure, a numerical dissipation source term  $S_D$  is added to the right-hand side of Eqs. (1-3):

$$S_D = \mu_2 \Delta^2(Q) - \mu_4 D_4 \Delta^4(Q), \quad \mu_2 = 0.14 \psi_2(\text{CFL}) \left| \frac{\Delta^2 P}{P_{\text{avg}}} \right|$$

$$\mu_4 = 0.014 \psi_4(\text{CFL}) \quad (17)$$

where  $\Delta^2$  and  $\Delta^4$  are second- and fourth-difference operators, respectively, on  $Q = [\rho, \rho u, \rho v, E]$  along the grid lines, and  $\Psi_2$  and  $\Psi_4$  are input coefficients with values typically set to 1.0. The fourth-difference dissipation is scaled by the coefficient  $D_4$ , which is proportional to the inverse of the absolute value of the mean strain rate squared:

$$D_4 = \min^2 \left[ 1.0, \frac{1}{\max(1 \times 10^{-5}, |(\partial u / \partial y) + (\partial v / \partial x)|)} \right] \quad (18)$$

This function decays the numerical dissipation in all viscous flow regions, including boundary layers, wakes, large eddies, secondary flows, etc. It has been found to work well for flows without as well as with heat transfer.

#### C. Decomposition, Parallelization, and Agglomeration

Decomposition of the computational domain is performed in a separate grid-generation procedure. This procedure generates a smooth, stretched computational grid using an algebraically generated initial grid that is smoothed with a multiblock Poisson technique [29,30]. Decomposition of the initial multiblock grid into additional grid blocks to enhance parallelization of the solution is performed using an optimization procedure that attempts to load-balance the resulting blocks as much as possible. The grid-generation procedure produces a computational grid file as well as the MBFLO global connectivity file that describes block-neighbor and boundary-condition information.

Parallel versions of the MBFLO suite of codes exist in addition to the serial versions. Parallelization is performed using the Message Passing Interface (MPI) library [31]. Message passing is limited to a single subroutine for each of the flow and turbulence solvers to reduce overhead and allow for scalable parallelization. Figure 1 shows the typical speedup as a function of the number of processors for the MBFLO2P code. The configuration used to generate this data was a turbine cascade similar to that shown subsequently in the Results section, in which the computational grid consisted of 34,000 grid points and 30 blocks. These data were generated on a Linux cluster consisting of 2.6 GHz Athalon CPUs. Figure 1 shows that a speedup factor of 25.5 is realized, with 30 processors yielding an 85% parallel efficiency, which is considered good for a two-dimensional procedure with this number of grid points. As a result, the computational turnaround time per grid point, per iteration using 30 processors, is  $2 \times 10^{-6}$  s. Typical time-averaged detached-eddy simulations of configurations with a similar grid density in which a steady RANS solution followed by an unsteady detached-eddy solution and time-averaging over an appropriate period can be performed in less than 1 h clock time.

It can be tedious to postprocess solutions in which the computational domain has been decomposed into many blocks. Creating continuous pressure distributions or integrating quantities requires knowledge of the block connectivity. Postprocessing could

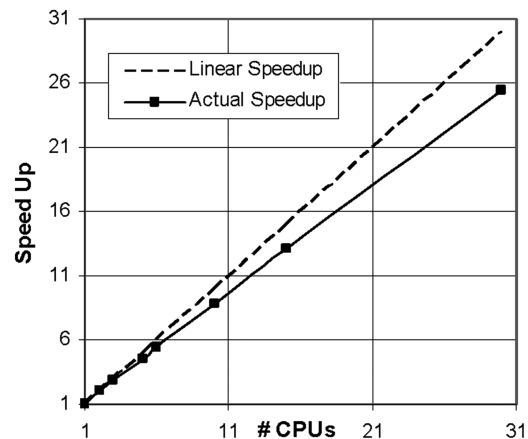
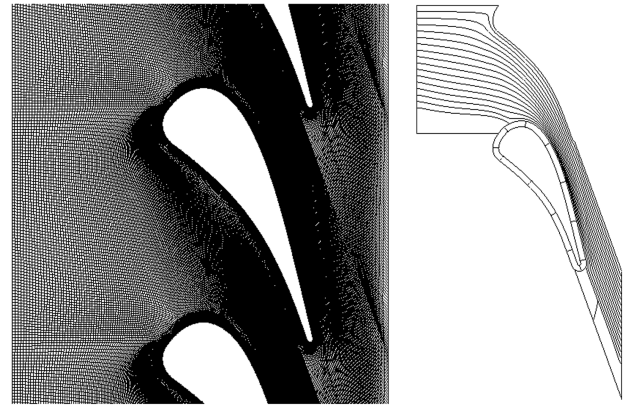


Fig. 1 Typical speedup factor as function of the number of processors.

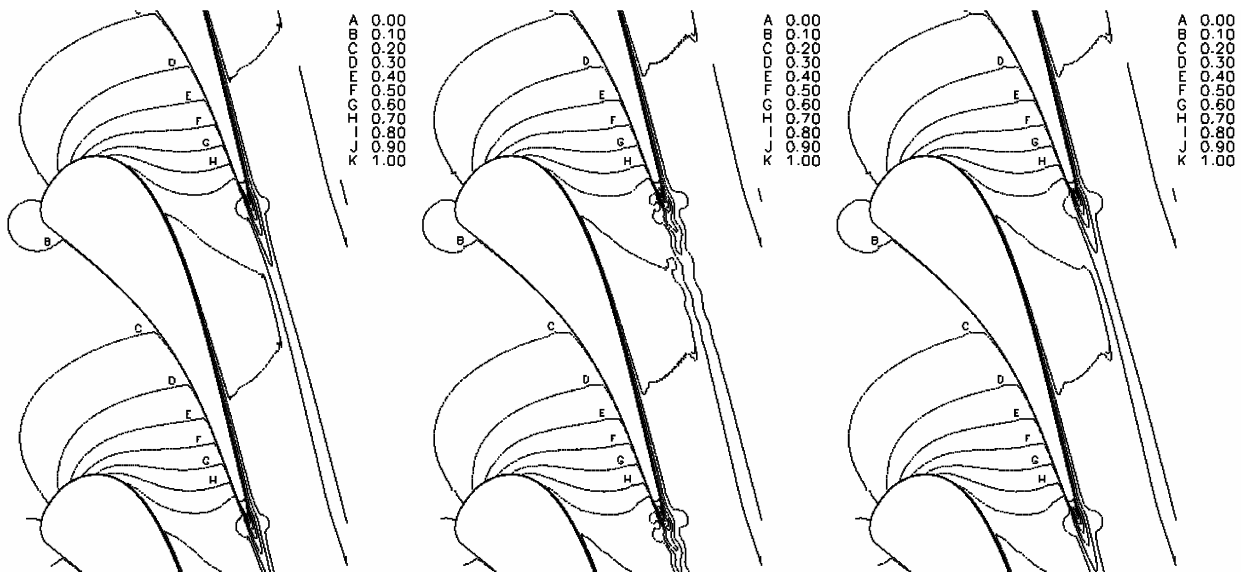
be done entirely within the flow solution procedure that stores this information. However, it is desirable to also be able to postprocess information in a separate procedure. To simplify this separate postprocessing step, the MBFLO procedure has the ability to agglomerate the decomposed set of blocks back to a minimal number of blocks. This ability greatly expedites the postprocessing of pressure distributions, boundary-layer characteristics, and aerodynamic performance quantities as well as simplifies boundary-layer transition modeling.

**D. Automation**

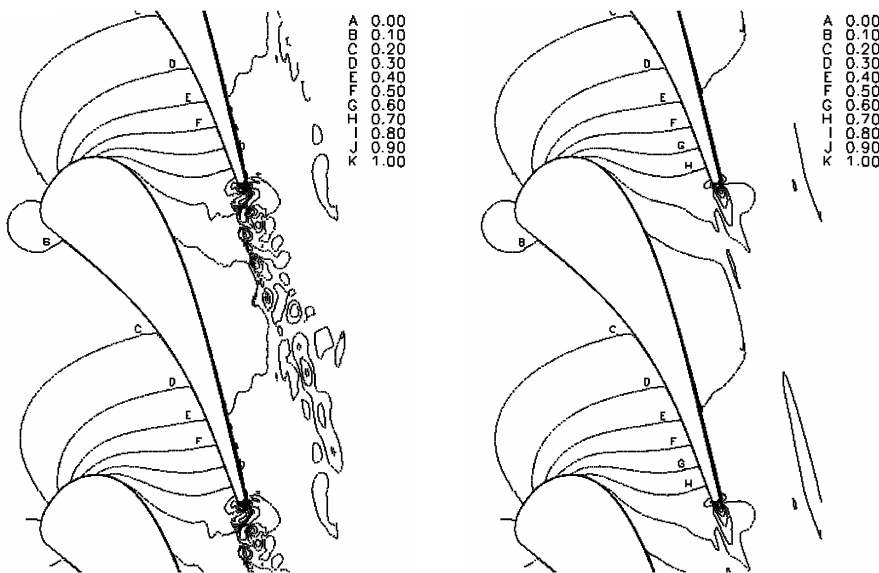
Several automation techniques were added to the MBFLO2P procedure in order to produce time-averaged detached-eddy simulation results in the same turnaround time as traditional steady Reynolds-averaged Navier–Stokes simulations. A detached-eddy simulation consists of the following automated steps to provide solution acceleration and the engineering information relevant to design:



a) Computational grid                      b) Computational blocks  
**Fig. 2 Turbine cascade computational grid and blocking scheme.**



a) Steady RANS                      b) Instantaneous RANS                      c) Time-averaged RANS



d) Instantaneous DES                      e) Time-averaged DES

**Fig. 3 Turbine cascade Mach number contours.**

- 1) Read global aerodynamic, connectivity, and computational grid information.
- 2) Define the initial conditions of all flow variables.
- 3) Perform decomposition of blocks to processors via processor restart files.
- 4) Each processor reads its own restart files consisting of individual connectivity, grid, and initial flow files.
- 5) Perform a steady Reynolds-averaged Navier–Stokes solution (used for comparison with the detached-eddy solution).
- 6) Write a global steady RANS solution file that is agglomerated back to a minimal number of blocks defined by the user to simplify postprocessing.
- 7) Continue with a time-accurate detached-eddy simulation for a specified number of time steps.
- 8) Over a prescribed time interval, time-average the detached-eddy simulation and write a global agglomerated instantaneous restart file for postprocessing and solution animation.
- 9) Write out the global time-averaged agglomerated detached-eddy simulation results.

**IV. Results**

The MBFLO2P code was verified with analytical data for a series of standard test cases such as steady inviscid flow over circular bumps and airfoils and viscous laminar and turbulent flow over a flat plate. The code was also validated against experimental data for viscous turbomachinery cascade flows and low-Reynolds number laminar flow over a circular cylinder. Turbulent simulation results using the MBFLO2P procedure are shown subsequently for turbomachinery applications to demonstrate accuracy and feasibility for use of the procedure in design.

**A. Turbine Cascade**

To demonstrate the solution capability of the RANS and DES procedures for flows at design conditions, the flow through the transonic turbine cascade tested by Arts et al. [32] was performed. Figure 2a shows the computational grid used in these simulations. The grid consisted of a total of 36,440 points. A 4-block HOHH grid was generated using a new cascade grid procedure in which an O-grid extends around the airfoil, an H-grid extends upstream and downstream of the O-grid leading and trailing edges, and an H-grid extends across the cascade passage. This 4-block grid was automatically decomposed further into 31 nearly equal-size blocks, all able to use the same multiple-grid levels for convergence acceleration. The outline of the 31 blocks is shown in Fig. 2b.

The flow conditions for the simulations shown subsequently correspond to test point MUR45, in which the inlet Mach number was 0.15 and the exit isentropic Mach number was 0.875. The inlet and exit flow angles relative to the horizontal are 0 and  $-75^\circ$ , respectively. The Reynolds number based on inlet conditions and axial chord is 115,400. Steady RANS, unsteady RANS, and DES simulations were performed to investigate the differences in solutions and to document the run times. The unsteady RANS and DES simulations were performed using the implicit dual-time-step procedure with a time-step size of  $2.4 \times 10^{-7}$  s. This time-step size was chosen in order to resolve any self-excited effects due to trailing-edge shedding. Approximately 100 time steps were performed for each trailing-edge shedding cycle. As a result, the unsteady

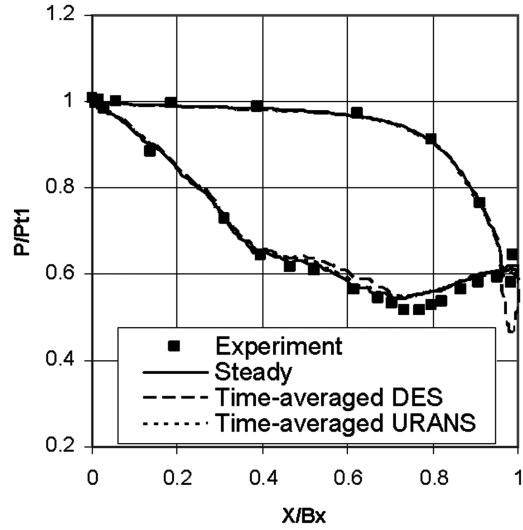


**Fig. 4 Turbine pressure distribution.**

simulations were run for a total of 8000 time steps, which corresponded to approximately 80 trailing-edge shedding cycles. The flow was time-averaged over the final 4000 time steps, or approximately 40 shedding cycles.

The Mach number contours from the steady RANS, instantaneous and time-averaged unsteady RANS (URANS), and instantaneous and time-averaged DES are shown in Figs. 3a–3e. In general, the Mach number contours of all simulations are similar, with the exception of the wake. The steady RANS contours show no wake shedding, due to the use of local time steps and multiple grids. The instantaneous URANS and DES contours show evidence of trailing-edge shedding, with the shedding much more well defined in the DES results.

Figure 4 shows a comparison between the steady RANS computed pressure distribution and the experimental data. All of the simulations produce similar pressure loading. The agreement between the simulations and the experimental pressure distribution is good except around the 75% axial chord positions on the suction side, where all simulations slightly overpredict the pressure. This overprediction is likely due to the assumed linear variation of spanwise stream-tube contraction in the simulations used to model the endwall boundary-layer effects in the experiment. The computed time-averaged DES pressure level is also slightly higher than the RANS results between 50–70% axial chord on the suction side downstream of the throat. This difference is likely due to the greater vortex shedding with corresponding mixing and reduced effective blockage in the wake of the DES simulation, as shown by comparisons of Figs. 3b and 3c with Figs. 3d and 3e. In addition, the time-averaged pressure is lower around the trailing edge, due to the stronger computed vortex shedding.

The total pressure loss coefficients

$$\zeta_2 = 1 - (P_2/P_{t2})^{\gamma/(\gamma-1)} / (P_2/P_{t1})^{\gamma/(\gamma-1)}$$

computed from the steady RANS, time-averaged DES, and time-averaged URANS (medium grid) are compared with the

**Table 1 Effect of grid density on computed total pressure loss coefficients (experimental value = 2.17)**

	Coarse grid (9,358 points) $\zeta_2$ loss coef, %	Medium grid (36,440 points) $\zeta_2$ loss coef, %	Fine grid (143,788 points) $\zeta_2$ loss coef, %
Steady RANS	6.54 (error = 4.37)	1.58 (error = -0.59)	3.15 (error = 0.98)
Time-averaged URANS	7.23 (error = 5.06)	1.81 (error = -0.36)	2.52 (error = 0.35)
Time-averaged DES	5.34 (error = 3.17)	2.20 (error = +0.03)	1.98 (error = -0.19)

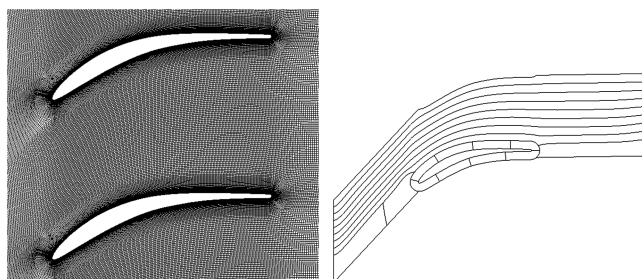
experimentally measured value in Table 1. The steady and time-averaged RANS computed loss is underpredicted. The DES loss coefficient is only very slightly overpredicted, with an error in exit nondimensionalized total pressure of only 0.03% or an error in loss coefficient of only 1.4%.

The results from these computations demonstrate that the time-averaged detached-eddy simulation methodology is better at predicting aerodynamic performance of the von Kármán Institute turbine. A grid-refinement study was performed to determine the sensitivity of the predictions to grid density. In addition to the preceding simulation results (denoted as medium with 36,440 points), steady URANS and DES simulations for grid densities approximately 4 times (2 times in each direction) more coarse (denoted coarse with 9,358 points) and 4 times more fine (denoted fine with 143,788 points) were performed. The wall spacing was kept the same for all cases in this investigation. Table 1 also gives the computed total pressure loss coefficients for the coarse- and fine-grid cases that can be compared with the medium-grid losses. Comparison shows that there are large variations in computed loss in the steady and time-averaged RANS simulations as a function of grid density, with the difference in computed loss coefficient being as much as 0.98%. Both steady and time-averaged RANS computed losses tend to overshoot the experimental value with grid refinement and converge to a fixed loss level in a roller-coaster fashion. The time-averaged DES simulations, however, asymptote to a loss coefficient that is close to the experimental data as the grid is refined.

## B. Compressor Cascade

The simulation of offdesign conditions is especially difficult for steady Reynolds-averaged Navier–Stokes procedures, due to the self-excited unsteadiness that arises from regions of separated flow. Like isolated airfoils, this mode of unsteadiness can also be especially large in turbomachinery axial compressors. Numerical techniques such as multiple-grid convergence acceleration as well as numerical dissipation can damp these modes of unsteadiness in steady simulations. Unsteady Reynolds-averaged procedures allow these unsteady modes to occur but can dampen the unsteady amplitude and create additional diffusion from the turbulence model. Detached-eddy simulation allows the resolved self-excited modes to occur without unnecessary turbulence modeling effects, thus increasing the accuracy of predicted unsteady amplitudes.

To demonstrate the capability to predict detached-eddy simulations of compressor cascades at offdesign, the flow through the cascade geometry designed and tested by Stephens and Hobbs [33] was performed. Details of the cascade geometry were given by Davis et al. [24]. The compressor cascade is shown in Fig. 5, along with the computational grid and parallel block decomposition used during the simulation. The agglomerated computational grid consisted of an O-grid around the airfoil with 385 (streamwise) by 33 (airfoil-normal) points, an upstream H-grid with 49 (streamwise) by 33 (tangential) points, a downstream H-grid with 81 (streamwise) by 17 (tangential) points, and a midpassage H-grid with 297 (streamwise)



a) Computational grid      b) Computational blocks  
**Fig. 5 Transonic compressor cascade computational grid and blocking scheme.**

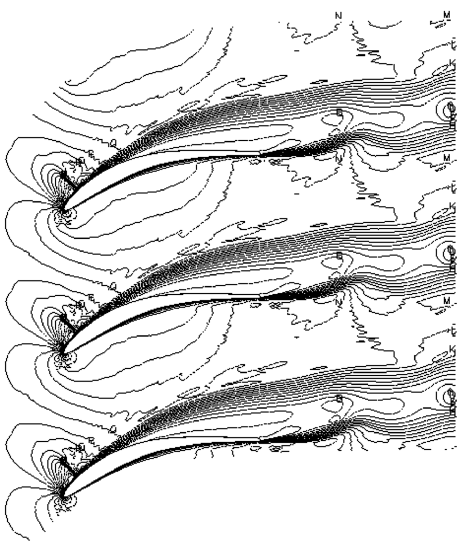
by 65 (tangential) points, for a total of 35,004 points. This is approximately 6 times the number of grid points used in the previous steady RANS simulations of Davis et al. [24].

The flow conditions for this simulation correspond to a positive incidence of 7 deg with an inlet angle of 50 deg, an exit angle of 0 deg (both relative to the horizontal), an inlet Mach number of 0.738, and an exit Mach number of 0.555. The inlet Reynolds number based on axial chord was 327,352. For these conditions, the flow is transonic near the leading edge and shocks due to suction-side stall off the blade at approximately 15% axial chord. The URANS and DES simulations were performed using a global time step of  $3.3 \times 10^{-7}$  s. A total of 20,000 time steps were run for these simulations, and the flow was time-averaged over the last 12,000 of these time steps. This test case illustrates how the global time-step size is determined in the current procedure from the highest frequency of interest in the flow (in this case, due to trailing-edge shedding), whereas the time-averaging period is determined from the lowest frequency in the flow (in this case, due to large-scale vortices associated with suction surface stall).

Figures 6a–6e show the predicted Mach number contours at these conditions from the steady RANS, instantaneous RANS, time-averaged RANS, instantaneous DES, and time-averaged DES simulations. The steady RANS contours show a strong shock on the suction surface near the leading edge, with subsequent separation occurring at approximately 25% axial chord. The time-averaged URANS and DES computed Mach number contours do not show a shock, but rather a distributed recompression. In comparison, the unsteadiness in the flow is dramatically illustrated by the complex vortex structure in the instantaneous URANS and DES results of Figs. 6b and 6d. The vortices produced in the URANS simulation tend to be larger and at a lower frequency than those of the DES simulation. In addition, the DES results show strong vortex shedding near the trailing edge that are not as pronounced in the URANS simulation.

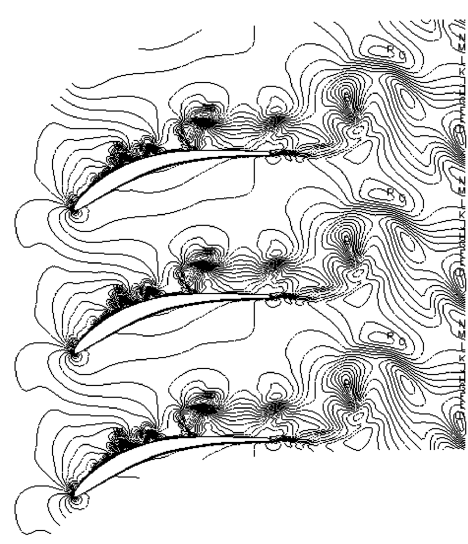
The computed total pressure loss coefficient  $(P_{t1} - P_{t2})/P_{t1}$  of the steady time-averaged URANS and time-averaged DES were 0.064, 0.069, and 0.067, whereas the experimental value was 0.044, indicating that all simulations overpredicted the loss due to the complex stalled flow. Prediction of the exact total pressure loss under these conditions is extremely difficult due to the exponential growth of total pressure loss as stall develops. The overprediction of loss in the RANS simulations is likely due to the double bookkeeping of the turbulence effects for the large vortical structures in the stalled-flow region and wake. The detached-eddy simulation reduced this double bookkeeping modeling error but still computed higher aerodynamic losses than the experimental data for this test case. This excessive loss level in the DES is probably due to the modeling coefficient  $C_{des}$  of Eqs. (15) and (16), which, as already pointed out, was found to be dependent on the freestream Reynolds number. Further validation simulations will likely help to better define this modeling coefficient.

A comparison of the computed steady and time-averaged pressure distribution with experimental data is shown in Fig. 6f. The steady pressure distribution exhibits a strong shock at 10% axial chord on the suction surface that, again, is not produced by the time-averaged URANS or DES simulations. The distributed recompression produced by both time-averaged simulations is in much better agreement with the experimental data on the suction surface. Both the time-averaged RANS and DES simulations underpredicted the pressure on the suction surface downstream of the transonic region (beyond 15% axial chord). Both simulations also overpredicted the pressure on the later portion of the suction surface. The agreement between the time-averaged RANS computed pressure and the experimental data is generally better, however, than that computed by the time-averaged DES simulation. The difference in predicted pressure levels is most likely due to the smaller vortical structures produced in the DES simulation as already mentioned and shown in Figs. 6b and 6d. The time-averaged URANS and DES simulation results agree well with the measured data on the pressure surface (upper curve of pressure distribution), whereas the steady RANS results underpredict the pressure toward the trailing edge.



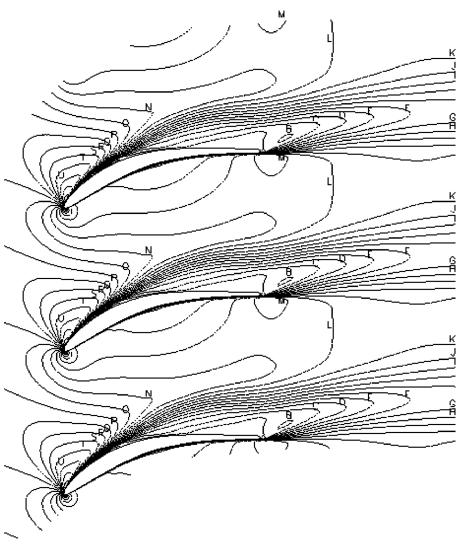
a) Steady RANS

A	0.00
B	0.05
C	0.10
D	0.15
E	0.20
F	0.25
G	0.30
H	0.35
I	0.40
J	0.45
K	0.50
L	0.55
M	0.60
N	0.65
O	0.70
P	0.75
Q	0.80
R	0.85
S	0.90
T	0.95
U	1.00
V	1.05
W	1.10
X	1.15
Y	1.20
Z	1.25
a	1.30
b	1.35
c	1.40



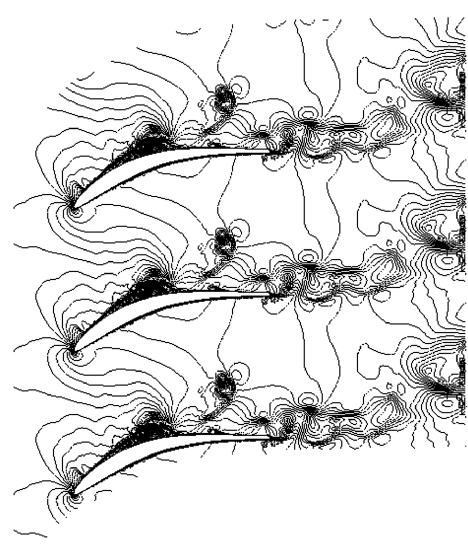
b) Instantaneous RANS

A	0.00
B	0.05
C	0.10
D	0.15
E	0.20
F	0.25
G	0.30
H	0.35
I	0.40
J	0.45
K	0.50
L	0.55
M	0.60
N	0.65
O	0.70
P	0.75
Q	0.80
R	0.85
S	0.90
T	0.95
U	1.00
V	1.05
W	1.10
X	1.15
Y	1.20
Z	1.25
a	1.30
b	1.35
c	1.40



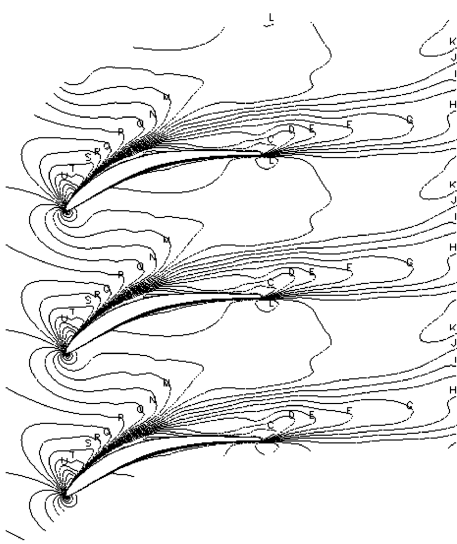
c) Time-averaged RANS

A	0.00
B	0.05
C	0.10
D	0.15
E	0.20
F	0.25
G	0.30
H	0.35
I	0.40
J	0.45
K	0.50
L	0.55
M	0.60
N	0.65
O	0.70
P	0.75
Q	0.80
R	0.85
S	0.90
T	0.95
U	1.00
V	1.05
W	1.10
X	1.15
Y	1.20
Z	1.25
a	1.30
b	1.35
c	1.40



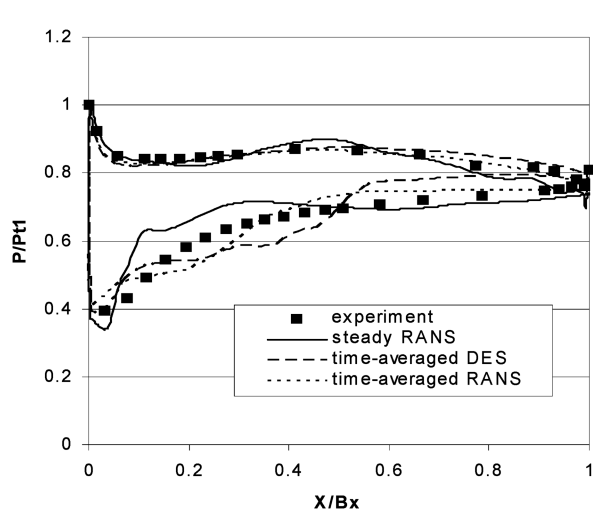
d) Instantaneous DES

A	0.00
B	0.05
C	0.10
D	0.15
E	0.20
F	0.25
G	0.30
H	0.35
I	0.40
J	0.45
K	0.50
L	0.55
M	0.60
N	0.65
O	0.70
P	0.75
Q	0.80
R	0.85
S	0.90
T	0.95
U	1.00
V	1.05
W	1.10
X	1.15
Y	1.20
Z	1.25
a	1.30
b	1.35
c	1.40



e) Time-averaged DES

A	0.00
B	0.05
C	0.10
D	0.15
E	0.20
F	0.25
G	0.30
H	0.35
I	0.40
J	0.45
K	0.50
L	0.55
M	0.60
N	0.65
O	0.70
P	0.75
Q	0.80
R	0.85
S	0.90
T	0.95
U	1.00
V	1.05
W	1.10
X	1.15
Y	1.20
Z	1.25
a	1.30
b	1.35
c	1.40



f) Pressure distribution

Fig. 6 Transonic compressor cascade Mach number contours.

## V. Conclusions

A new parallel two-dimensional detached-eddy simulation procedure, MBFLO2P, was developed for the efficient solution of time-averaged turbulent flow of general configurations. The goal of this effort was to develop an accurate turbulent-flow procedure capable of producing time-averaged detached-eddy solutions in approximately the same wall-clock time as previous steady Reynolds-averaged solutions. Efficient parallelization and automation techniques were incorporated to help reach this goal. Results are shown that demonstrate the ability of the current procedure to accurately and rapidly compute unsteady and time-averaged turbulent flow of turbomachinery cascades at design and offdesign conditions, making the procedure eligible for use in design.

## Acknowledgments

The authors would like to thank John Clark and the managers of the turbine branch at the U.S. Air Force Research Laboratory (Wright-Patterson Air Force Base, Ohio) for their support of this effort under contract 03-S530-0002-11-C1. The first author would also like to thank graduate students Radoslav (Ronny) Bozinoski and Andrew Andrade for their helpful discussions.

## References

- [1] Davis, R. L., "Challenges for CFD in Gas-Turbine Applications," *14th Annual Conference of the Computational Fluid Dynamics Society of Canada* [CD-ROM], CFD Society of Canada, Kingston, Ontario, Canada, July 2006, Paper 1216.
- [2] Venkatakrishnan, V., and Allmaras, S., "Higher Order Schemes for the Compressible Navier-Stokes Equations," AIAA Paper 2003-3987, 2003.
- [3] Ekaterinaris, F., "On the Use of High Order Methods for Complex Aerodynamic Problems," AIAA Paper 2004-431, 2004.
- [4] Mawlood, M., "Flux Limiting with High-Order Compact Schemes," AIAA Paper 2005-607, 2005.
- [5] Ramboer, J., Smirnov, S., and Lacor, C., "Finite Volume Formulation of Compact Upwind Schemes for CAA and LES Applications," AIAA Paper 2003-3967, 2003.
- [6] Touloupoulos, I., and Ekaterinaris, J., "High-Order Discontinuous-Galerkin Discretizations for Computational Aeroacoustics in Complex Domains," AIAA Paper 2004-522, 2004.
- [7] Yao, J., Davis, R. L., Alonso, J. J., and Jameson, A., "Massively Parallel Simulation of the Unsteady Flow in an Axial Turbine Stage," *Journal of Propulsion and Power*, Vol. 18, No. 2, Mar.-Apr. 2002, pp. 465-471.
- [8] van der Weide, E., Kalitzin, G., and Alonso, J., "Unsteady Turbomachinery Computations Using Massively Parallel Platforms," AIAA Paper 2006-421, Jan. 2006.
- [9] Wilcox, D. C., "Formulation of the  $k-w$  Turbulence Model Revisited," AIAA Paper 2007-1408, Jan. 2007.
- [10] Olsen, M. E., and Coakley, T. J., "The Lag Model, a Turbulence Model for Non Equilibrium Flows," AIAA Paper 2001-2564, 2001.
- [11] Menter, F., Kuntz, M., and Bender, R., "A Scale-Adaptive Simulation Model for Turbulent Flow Predictions," AIAA Paper 2003-0767, 2003.
- [12] Menter, F., and Egorov, Y., "A Scale-Adaptive Simulation Model Using Two-Equation Models," AIAA Paper 2005-1095, 2005.
- [13] Strelets, M., "Detached Eddy Simulation of Massively Separated Flows," AIAA Paper 2001-879, Jan. 2001.
- [14] Bush, R. H., and Mani, M., "A Two-Equation Large Eddy Stress Model for High Sub-Grid Shear," AIAA Paper 2001-2561, June 2001.
- [15] Smagorinsky, J., "General Circulation Experiments with the Primitive Equations," *Monthly Weather Review*, Vol. 91, No. 3, pp. 99-164. doi:10.1175/1520-0493(1963)091<0099:GCEWTP>2.3.CO;2
- [16] Lesieur, M., and Metais, O., "New Trends in Large Eddy Simulations of Turbulence," *Annual Review of Fluid Mechanics*, Vol. 28, 1996, pp. 45-82. doi:10.1146/annurev.fl.28.010196.000401
- [17] Boris, J. P., Grinstein, F. F., Oran, E. S., and Kolbe, R. L., "New Insights into Large Eddy Simulation," *Fluid Dynamics Research*, Vol. 10, Nos. 4-6, 1992, pp. 199-229. doi:10.1016/0169-5983(92)90023-P
- [18] Germano, M., Piomelli, U., Moin, P., and Cabot, W. H., "A Dynamic Subgrid-Scale Eddy Viscosity Model," *Physics of Fluids*, Vol. 3, July 1991, pp. 1760-1765. doi:10.1063/1.857955
- [19] Wilcox, D. C., "Reassessment of the Scale-Determining Equation for Advanced Turbulence Models," *AIAA Journal*, Vol. 26, No. 11, 1988, pp. 1299-1310. doi:10.2514/3.10041
- [20] Wilcox, D. C., *Turbulence Modeling for CFD*, DCW Industries, Inc., La Canada, CA, 1998.
- [21] Ni, R. H., "A Multiple Grid Scheme for Solving the Euler Equations," *AIAA Journal*, Vol. 20, No. 11, 1982, pp. 1565-1571. doi:10.2514/3.51220
- [22] Dannenhoffer, J. F., "Grid Adaptation for Complex Two-Dimensional Transonic Flows," Dept. of Aeronautics and Astronautics, Massachusetts Inst. of Technology, Rept. CFDL-TR-87-10, Cambridge, MA, Aug. 1987.
- [23] Davis, R. L., Ni, R. H., and Carter, J. E., "Cascade Viscous Flow Analysis Using the Navier-Stokes Equations," *Journal of Propulsion and Power*, Vol. 3, No. 5, Sept.-Oct. 1987, pp. 406-414.
- [24] Davis, R. L., Hobbs, D. E., and Weingold, H. D., "Prediction of Compressor Cascade Performance Using a Navier-Stokes Technique," *Journal of Turbomachinery*, Vol. 110, No. 4, 1988, pp. 520-531.
- [25] Jameson, A., "Time Dependent Calculations Using Multi-Grid, with Applications to Unsteady Flows Past Airfoils and Wings," AIAA Paper 91-1596, June 1991.
- [26] Spalart, P. R., "Young Person's Guide to Detached-Eddy Simulation Grids," NASA CR-2001-211032, 2001.
- [27] Jameson, A., Schmidt, W., and Turkel, E., "Numerical Solutions of the Euler Equations by Finite Volume Methods Using Runge-Kutta Time-Stepping Schemes," AIAA Paper 81-1259, June 1981.
- [28] Chima, R. V., "Inviscid and Viscous Flows in Cascades with an Explicit Multiple-Grid Algorithm," *AIAA Journal*, Vol. 23, No. 10, 1985, pp. 1556-1563.
- [29] Sorenson, R. L., "A Computer Program to Generate Two-Dimensional Grids About Airfoils and Other Shaped by the Use of Poisson's Equation," NASA TM-81198, 1980.
- [30] Thompson, J. F., Thames, F. C., and Mastin, C. W., "Automatic Numerical Grid Generation of Body-Fitted Curvilinear Coordinate System for Field containing Any Number of Arbitrary Two-Dimensional Bodies," *Journal of Computational Physics*, Vol. 15, No. 3, July 1974, pp. 299-319.
- [31] Gropp, W., Lusk, E., and Skjellum, A., *Using MPI, Portable Parallel Programming with the Message-Passing Interface*, MIT Press, Cambridge, MA, 1999.
- [32] Arts, T., Lambert de Rouvroit, M., and Rutherford, A. W., "Aero-Thermal Investigation of a Highly Loaded Transonic Linear Turbine Guide Vane Cascade," von Kármán Institute for Fluid Dynamics, TN 174, Rhode Saint Genèse, Belgium, Sept. 1990.
- [33] Stephens, H. E., and Hobbs, D. E., "Design and Performance Evaluation of Supercritical Airfoils for Axial Flow Compressors," Naval Air Systems Command Rept. FR11455, Patuxent River, MD, June 1979.

F. Liu  
Associate Editor